JGR Atmospheres

RESEARCH ARTICLE
10.1029/2022JD037053

Sensitivity of Deep Convection and Cross-Tropopause Water Transport to Microphysical Parameterizations in WRF

Apoorva Pandey[1], Fayçal Lamraoui[2], Jessica B. Smith[1], Corey E. Clapp[1], David S. Sayres[1], and Zhiming Kuang[1,2]

[1]Harvard John A. Paulson School of Engineering and Applied Sciences, Harvard University, Cambridge, MA, USA, [2]Department of Earth and Planetary Sciences, Harvard University, Cambridge, MA, USA

Key Points:

- Significant sensitivity of mid-latitude deep convective storm and the associated anvil cirrus cloud to choice of model microphysics schemes
- Hydrometeor size-dependent microphysical process are linked with large variability in storm dynamics
- Six bulk microphysics schemes produced an order of magnitude spread in above-tropopause water vapor concentrations

Supporting Information:

Supporting Information may be found in the online version of this article.

Correspondence to:

A. Pandey,
apoorva@huarp.harvard.edu

Citation:

Pandey, A., Lamraoui, F., Smith, J. B., Clapp, C. E., Sayres, D. S., & Kuang, Z. (2023). Sensitivity of deep convection and cross-tropopause water transport to microphysical parameterizations in WRF. *Journal of Geophysical Research: Atmospheres*, *128*, e2022JD037053. https://doi.org/10.1029/2022JD037053

Received 4 MAY 2022
Accepted 29 MAY 2023

Author Contributions:

Conceptualization: Apoorva Pandey, Jessica B. Smith, Corey E. Clapp, David S. Sayres
Formal analysis: Apoorva Pandey, Fayçal Lamraoui
Investigation: Apoorva Pandey
Methodology: Apoorva Pandey, Fayçal Lamraoui
Supervision: Zhiming Kuang
Validation: Zhiming Kuang
Writing – review & editing: Jessica B. Smith, Corey E. Clapp, David S. Sayres, Zhiming Kuang

Abstract Deep convective storms can overshoot the tropopause, thus altering the composition of the stratosphere by vertically transporting tropospheric air. The transport of water vapor and ice particles into a sub-saturated environment can hydrate the stratosphere, with implications for radiative forcing and ozone chemistry. Cloud-resolved models, if employed at high spatial resolutions, are used to probe process-level questions about cross-tropopause deep convective hydration and its controls. There is considerable diversity in model representations of processes associated with water transport and transformation, and the choice of a microphysics scheme affects model skill in simulating deep convective events. This motivates our evaluation of state-of-the-art, as well as widely used standard schemes, in a high spatial- and temporal-resolution framework. Six bulk microphysics schemes were employed in a WRF-LES setup, initialized with a sounding profile representative of a tropopause-overshooting storm. We used an idealized framework to isolate the effect of microphysics on the dominant processes that control the reach of deep convection and stratospheric hydration. All schemes produced the highest reaching updrafts 8–12 hr into the simulation but the strength and persistence of updrafts varied across the schemes; maximum storm heights ranged 9.1–12.6 km across the schemes. Varying microphysics produced large differences in the vertical extent and horizontal aggregation of convection, and an order of magnitude spread in above-tropopause water vapor concentrations.

Plain Language Summary Strong thunderstorms often result in deep convection, by generating vertical winds that transport water and air from the troposphere into the stratosphere. The resulting moistening of the stratosphere can impact the radiative budget in that region and impact ozone chemistry. Satellite and aircraft based measurements have provided evidence of increased moisture in the lower stratosphere due to deep convective storms but there remain many gaps in our process level understanding of such observations. Informative simulations of convective storms require an understanding of how the dynamic representation of transformations of water in vapor, liquid and frozen forms in cloud-resolving models affects model skill in generating convection. This study uses an idealized setup to investigate the performance of six different microphysical schemes and finds that microphysics mediate large differences in storm dynamics and associated stratospheric moistening.

1. Introduction

The transport of moist air into the upper troposphere and lower stratosphere (UTLS) occurs through different pathways; among them, convective overshooting has been identified as an important source of stratospheric moistening over North America (e.g., Jensen et al., 2020; Randel & Park, 2019; Yu et al., 2020). The transport of water vapor by convective overshoots that reach the lower stratosphere can have a radiative effect on climate (Banerjee et al., 2019; Dessler et al., 2013; Shindell, 2001) and influence the chemistry of stratospheric ozone (Anderson et al., 2012, 2017; Hanisco et al., 2001; Shindell, 2001). Aircraft (e.g., Khaykin et al., 2022; Smith et al., 2017), balloon (Khaykin et al., 2016; Khordakova et al., 2022), and satellite (Homeyer et al., 2017; Jensen et al., 2020) observations provide evidence of cross-tropopause deep convective hydration but there remain questions regarding the amount, vertical and horizontal extent of moistening and the processes that control its evolution. Case studies of convective storms using cloud resolving models (CRMs) with sophisticated parameterizations, like the widely used Weather Research and Forecasting (WRF) model (Powers et al., 2017; Skamarock et al., 2019), can help fill some of the process-level knowledge gaps. To that end, it is necessary to evaluate key considerations in setting up a suitable model of deep convection. Recent studies have highlighted the need for high horizontal and vertical resolution, particularly in the upper troposphere-lower stratosphere (UTLS) region (Dauhut et al., 2014;

Qu et al., 2020). Systematic analyses of the relationship between spatial resolution and skill in modeling convective processes show that grid spacing of the order of a few hundred meters is needed to effectively simulate deep convective events. At Large-Eddy Simulations (LES) scale, the model is assumed to explicitly resolve the largest, most energetic "eddies" that are responsible for most of the turbulent transport (Moeng & Sullivan, 2015).

In addition to model resolution, the choice of microphysics schemes governs the formation, growth, and depletion of ice-phase hydrometeors and therefore, impacts the development of thunderstorm-driven overshoots above the tropopause (e.g., Phoenix et al., 2017; Xue et al., 2017). Microphysics schemes are simplified representations of the liquid and frozen hydrometeor populations in the model. The widely used bulk microphysics schemes (BMPs) predict one or more moments of the hydrometeor distribution (e.g., mixing ratio, number concentration, volume). These schemes employ observations-based assumptions and some ad-hoc tuning factors that govern the hydrometeor properties and their evolution. Across the commonly used BMPs, there is a significant variation in the number of hydrometeor categories, size distribution and ice shape options as well as the number of prognostic moments, that is, predicted bulk properties (Skamarock et al., 2019). This variation reflects the difficulties associated with developing microphysical parameterizations, and relatedly, a paucity of comprehensive observational constraints (Shan et al., 2020; Straka, 2009). Ice-phase microphysics are particularly challenging because unlike liquid droplets, ice particles have a wide range of sizes (spanning 7 orders of magnitude), densities and complex shapes that affect their growth, sublimation and sedimentation rates (Lin et al., 2021).

Idealized case studies can be used to elucidate the effects of microphysics on specific aspects of a scenario of interest. Such simulations enable simpler interpretation, aiding the comparison of different microphysical parameterizations under similar initial dynamical conditions (Tao et al., 2016). Idealized 2-D squall line simulations widely used for microphysics intercomparisons (Bao et al., 2019; Bryan & Morrison, 2012; Morrison et al., 2009; Van Weverberg et al., 2012) generally indicate that schemes that predict mass and number concentrations of hydrometeors perform better than those that only predict mass mixing ratios. It is unclear if those findings hold more broadly (3-D setups and/or other meteorological scenarios): in an idealized simulation of a tropical cyclone (Bao et al., 2016), the variation in spectral definition of hydrometeor categories affected the performance more significantly than the number of predicted properties of the hydrometeor distribution. Limitations and deficiencies of microphysics schemes, identified through assessments such as those mentioned above, have been addressed in successive iterations (Powers et al., 2017; Skamarock et al., 2019). This may be done by introducing new species/processes that are parameterized using tunable parameters, and fixing ad-hoc values that perform reasonably for a test case (Tapiador et al., 2019). Broadly, recent bulk-microphysics improvement efforts have adopted one of two distinct approaches: (a) the provision of a larger set of frozen hydrometeor "types" (like subdivisions within rimed ice) and/or prediction of two or more moments of the hydrometeor distribution (Bae et al., 2019; Mansell et al., 2010; Morrison et al., 2009) or (b) the treatment of frozen as one category with continuously evolving properties, such as rime volume or particle density (Jensen et al., 2017, 2018a; Morrison & Milbrandt, 2015). The effect of these developments can be expected to depend on the meteorological scenario and the output variables of interest. In general, it is unclear whether incorporating greater complexity by increasing the number of hydrometeor categories leads to a clear improvement in scheme performance. This is because increasing complexity involves the use of a larger number of uncertain conversion processes and parameters. Various two- and three-moment bulk microphysical schemes involve different dimensions of increased complexity, and therefore, variability in their performance is very likely.

As a step toward employing sophisticated CRM simulations to better understand deep convection and its effect on UTLS hydration, it is important to evaluate state-of-the-art, as well as widely used standard schemes, in a high spatial- and temporal-resolution framework. Further, given the well-known links between microphysics and cloud dynamics (Grabowski, 2014, 2015; Xue et al., 2022), it is beneficial to understand the dominant processes that control deep convection, along with other factors that affect UTLS hydration due to overshooting deep convection. With that motivation, this work aims to (a) contrast the evolution of hydrometeor profiles for diverse microphysics representations, (b) link microphysical differences with associated variations in the (diabatic and radiative) energetics of the simulated storms, and finally (c) quantify the spread in UTLS hydration attributed solely to changes in microphysics parameterizations. Here, we use an LES-scale idealized simulation with six distinct bulk microphysics parameterizations to evaluate the effect of varying microphysics on the development of a deep convective event (i.e., dynamics effects of varying microphysics) and the associated hydration at and above the cold-point tropopause level. All simulations are driven by a sounding profile associated with a tropopause-overshooting supercell convection event (Barth et al., 2015; Homeyer et al., 2017)

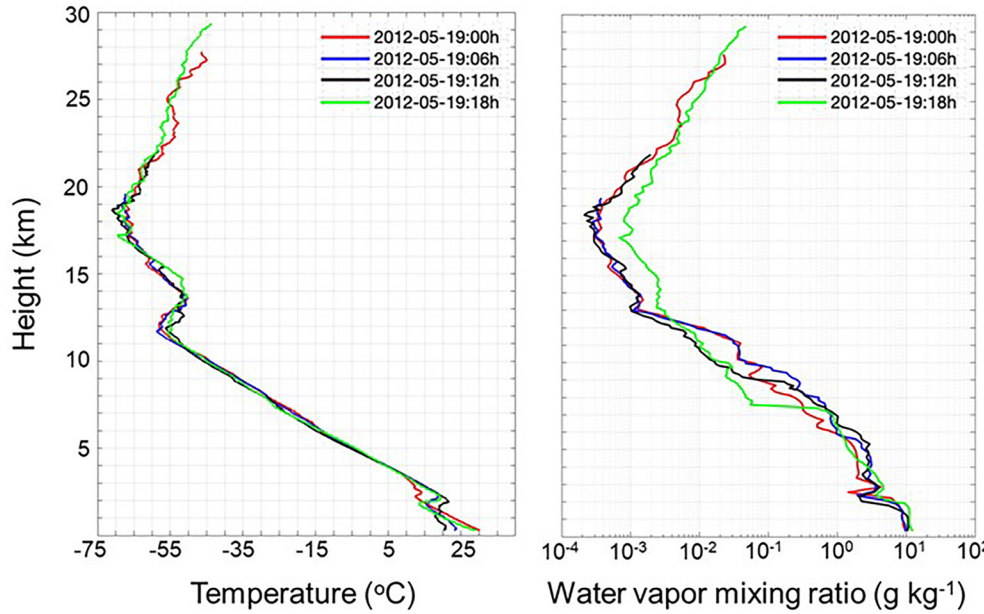

Figure 1. Temperature (left) and water vapor (right) sounding profiles from the ARM-SGP Lamont (OK) site on 20 May 2012.

observed over central Oklahoma on May 19th–20th 2012, as part of the Deep Convective Clouds & Chemistry Experiment (DC3) campaign. We chose a small-domain setup that allowed for a grid spacing of 100 m in all dimensions—a resolution at which cloud-scale motions, and transport and mixing into the convective core—are adequately resolved. With the use of the selected ideal case study, we aimed to generate a strong convective updraft that reaches the tropopause. Given the semi-idealized setup, the reproduction of the observed storm was not a goal of this study. Instead, our goal was to conduct a case study that generates deep convection (i.e., provides enough updraft to bring water vapor and hydrometeors to the tropopause), in order to elucidate how different microphysical parameterizations handle moisture and frozen hydrometeors at the tropopause using the same initial conditions.

2. Materials and Methods

2.1. Experiment Design

The numerical experiments consist of a set of three-and two-dimensional LES simulations initialized by the same soundings obtained from an ARM-SGP (Atmospheric Radiation Measurement Program-Southern Great Plains) site (Lamont, OK) during the DC3 Field Campaign (Barth et al., 2015) at 1800 UTC 20 May 2012, with no horizontal advection. The simulations are configured using a single thermodynamic profile, spatially homogenous forcing, and doubly periodic lateral boundary conditions to constrain the solutions to be periodic in both horizontal directions. In practice, this means that air masses leaving one side of the domain reenter the opposite side (for a visual demonstration of this see Figure S1 in Supporting Information S1). Model configurations with periodic boundary conditions applied to small domains are frequently used to approximate the behavior of large domains (Gustafson Jr et al., 2020; Ovchinnikov et al., 2022). With the above forcing and boundary condition idealizations, the model is not expected to produce a realistic case study. However, such a design is a computationally feasible tool for analyzing the effect of specific model choices—in this case, bulk microphysical parameterizations.

Among the double tropopause 6-hourly profiles (Figure 1) that are available at Lamont (ARM-SGP) site on 19 May 2012, the 1800 UTC one is selected because it reaches the highest altitude of all available profiles. The idealized simulations were performed using the Weather Research and Forecasting Model (WRF) with the Advanced Research core version 4.2 (WRF-ARW; Skamarock et al., 2019) spanning 15-hr integration, run on the Cannon high performance computing cluster of Harvard University. The first 4 hr were discarded as spinup.

Table 1
A Summary of the Frozen Hydrometeor Species and Distributions of Prognostic Variables in the Six Microphysics Schemes Used in This Study

	Frozen hydrometeor categories and distributions									
	Jensen		Morrison		NSSL		P3	Thompson		WDM7
Species	Ice		Ice		Ice		Ice	Ice		Ice
		Planar	Snow		Snow			Snow		Snow
		Columnar	Graupel		Graupel			Graupel		Graupel
		Aggregates								Hail
Prognostic variables	Number, mass distributions for all		Number, mass distributions for all		Number, mass distributions for all		Number, mass, rime growth mass and bulk rime volume	Number, mass distributions for ice		Mass distributions for all
	Two volume-dimensioned mixing ratio distributions for planar and columnar ice							Mass distributions for snow and graupel		CCN number concentration predicted

Cross-tropopause overshooting deep convection is associated with a significant coupling between all atmospheric layers from the surface to the tropopause. Although the Upper Troposphere - Lower Stratosphere (UTLS) is the target of investigation here, dynamical, and microphysical developments in the UTLS depend on the conditions in the bulk of the troposphere. For the 3-D simulations, a 100-m vertical and horizontal grid spacing was imposed on the entire atmospheric column to ensure an adequate transition of deep convection through different life stages and atmospheric layers before reaching the tropopause. A sponge layer (Dauhut et al., 2018; Kawashima, 2021; Potter & Holton, 1995) was implemented within the upper 5 km of the domain to attenuate gravity waves and prevent them from being reflected at the model top. The spatial domain of the 3-D simulations was 50 km × 50 km × 30 (or 500 × 500 × 300 grid points) and the output frequency was 5 min. Due to limitations in the computational and storage resources, domain size and resolution are two conflicting requirements. For this study, priority was given to spatial and temporal resolutions at the expense of domain size. Detailed sensitivity studies on model domain and dimensionailty setups indicate that 3-D simulations are necessary for adequately simulating convective updrafts (Petch, 2006; Phillips & Donner, 2006). Specifically, Phillips and Donner (2006) conducted 2-D and 3-D simulations of five observed cases of deep convection and found that ascent rates in cloudy updrafts were significantly higher in the 3-D runs, while weak ascent outside the updrafts was much less prevalent. These differences in simulated storm dynamics were also found to affect cloud microphysics: snow production, being a relatively slow process was favored in 2-D runs while graupel production was favored in the more intense updrafts of the 3-D simulations. Further, Petch (2006) recommend a minimum benchmark simulation with a resolution of 200 m and 25 km horizontal domain size. Domain configurations using 100 m horizontal grid spacing and 25 km domain size have also been employed for multiple cloud simulation intercomparison studies (Gustafson Jr et al., 2020 and references therein). With the chosen domain size, realistic simulations of a supercell storm are not possible. Instead, the idealized experimental design allows us to analyze the effects of microphysics during the first 15 hr of storm evolution—directly, and through interactions with dynamics—while minimizing the confounding effects of insufficient model resolution. Several studies have simulated deep convection with large domains, but to our knowledge, previous studies have not used a comparably high spatial resolution in all three dimensions (dx = dy = dz = 100 m), covering an atmospheric column of 30 km. Due to a limitation of computational resources, we configured our high resolution 3-D numerical experiment with a domain size that is less than ideal for deep convection events. To ensure that the essential properties of deep convection were captured, a second configuration was employed with a larger 2-D domain. This additional 2-D setup has a reasonable domain size for deep convection events but employed at a slightly coarser spatial resolution. This experiment served as a validation for our chosen study design: based on the 2-D experiment results, the small domain 3-D setup is not expected to confound our observations of the relative performance of different microphysical schemes. The additional 2-D large-domain (x-axis = 200 km, z-axis = 30 km) simulation was carried out only with Jensen microphysics scheme, horizontal grid spacing of 200 m and vertical grid spacing of 100 m. All other simulation details were identical to the 3-D small domain simulations.

2.2. Microphysics Schemes

The above configurations were fixed while microphysics schemes were varied. Six distinct bulk schemes (Table 1) were used: the Jensen Ice-Spheroids Habit Model with Aspect-ratio Evolution (ISHMAEL) bulk microphysics scheme (Jensen et al., 2017, 2018a, 2018b), "Jensen" hereafter, Morrison scheme (Morrison et al., 2009), National Severe Storms Laboratory (NSSL) scheme (Mansell et al., 2010), P3 (Morrison & Milbrandt, 2015), Thompson scheme (Thompson & Eidhammer, 2014) and WRF Double-Moment 7 (WDM7) scheme (Bae et al., 2019). Typical two-moment schemes (Morrison, NSSL and Thompson) predict liquid and frozen hydrometeor mass and number densities, thus allowing for the representation of a wider range of particle characteristics (details in Table 1). WDM7 is double-moment for liquid-phase

hydrometeors but predicts only the mass mixing ratio of frozen hydrometeors. The number concentration of ice is estimated based on the mass mixing ratio. Two of the schemes tested here (P3 and Jensen) are based on the idea that partitioning ice-phase particles into a limited number of categories is an inherently artificial, highly simplified representation of nature. Further, the larger number of categories in increasingly complex schemes implies an increase in the number of uncertain conversion processes and parameters. Thus, these two schemes feature a continuous evolution of frozen hydrometeors (unrimed and rimed), with explicit consideration of particle shape (or habit) only in the Jensen scheme.

Each of the six WRF runs produced 15 output files (one for each hour from for $t = 0$ hr to $t = 14$ hr) in Network Common Data Form (NetCDF) format. These output files are generated at a 5 min frequency. Output files (size ∼200 GB per file) were stored on the Harvard University cluster. Domain statistics (such as average or percentile values) were calculated for selected variables and further averaged and/or subsetted in the time dimension, using MATLAB version 2021a. These compressed representations of the model output were used for generating the figures in the subsequent section.

3. Results

In this section, we first discuss inter-scheme differences in the evolution of frozen water path over the simulation period. This is followed by a discussion of frozen hydrometeor mixing ratios in the 3-D simulations performed with the six microphysics schemes (Section 3.1), as well as in the large domain 2-D simulation (Section 3.2). We also highlight frozen hydrometeor bulk categories (where applicable) and associated properties which are salient to storm evolution. Section 3.3 focuses on the role of latent and radiative heating in modulating storm dynamics, through their effects on updrafts and in-cloud motions. Finally, our findings on the differences in UTLS hydration are presented in Section 3.4.

We describe below the integrated development of deep convection for each microphysics scheme at 15 hr. The evolution of ice-phase clouds is subdivided into three growth stages of deep convection using the following ranges of frozen water path: deep convection (FWP > 1,000 gm^{-2}), thick anvil (1,000 > FWP > 10 gm^{-2}), and thin cirrus (10 > FWP > 0.1 gm^{-2}) (Sokol & Hartmann, 2020). A total frozen water path (FWP), that includes all frozen hydrometeors, was calculated for each column of the grid. Typically, a convective system is initiated as a narrow core of deep convection. As convection matures, anvil clouds are detrained and spread horizontally (Gasparini et al., 2019; Houze Jr., 2004; Sokol & Hartmann, 2020). Typically, thick anvils exhibit a mode at FWP ∼30 gm^{-2} (Sokol & Hartmann, 2020). Finally, the anvil clouds break up and dissipate, in a stage marked with slow sedimentation and dominance of sublimation over other microphysical processes (Gasparini et al., 2019). Thus, for a typical storm with all the above stages (birth, mature and decay), the FWP should indicate a bi-modal distribution with peaks at the thick and thin (∼2 g m^{-2}) anvil stages (Sokol & Hartmann, 2020).

The results of six 15-hr simulations with different BMPs show that the evolution of FWP is highly sensitive to changes in microphysics. Figure 2 shows how storms simulated using the Morrison, NSSL, P3 and Thompson schemes evolved differently from those using the Jensen and WDM7 schemes. For Jensen and WDM7 schemes, the mature stage of deep convection is persistent even after 15 hr of the simulation. The storm has not yet reached the decay stage and therefore, a unimodal FWP distribution is observed. The WDM7 simulation appears to be entering the decay phase, with a peak forming within the thin cirrus range. More information could be gleaned by running longer simulations with the above schemes, but due to computational costs, we restrict our comparisons to the 15-hr simulations. The Morrison scheme indicates the highest frequency of thin cirrus, followed by the P3 scheme. The NSSL scheme is dominated by thick anvil. These three schemes exhibit a typical bimodal distribution representing a complete storm life cycle. The NSSL distribution is dominated by 80% of thick anvil and only 12% of thin cirrus, indicating faster depletion and sedimentation of frozen hydrometeors. It should be noted that the distributions at storm completion (which is longer than 15 hr for some of these simulations) for each case would likely be different.

The anvil mode peak in the NSSL simulation is shifted rightward to FWP ∼350 g m^{-2}. In following sections, we show that the NSSL simulation is dominated by thick, shallow clouds. Time-series of the FWP evolution (domain-means) for each of these schemes is shown in Figure 3. While the mean FWP for most of the schemes (with the exception of Jensen and NSSL) exhibits decline after $t = 10$ hr, each of the simulations still has significant frozen water content toward the end of the simulation period. While this study does not follow all simulations

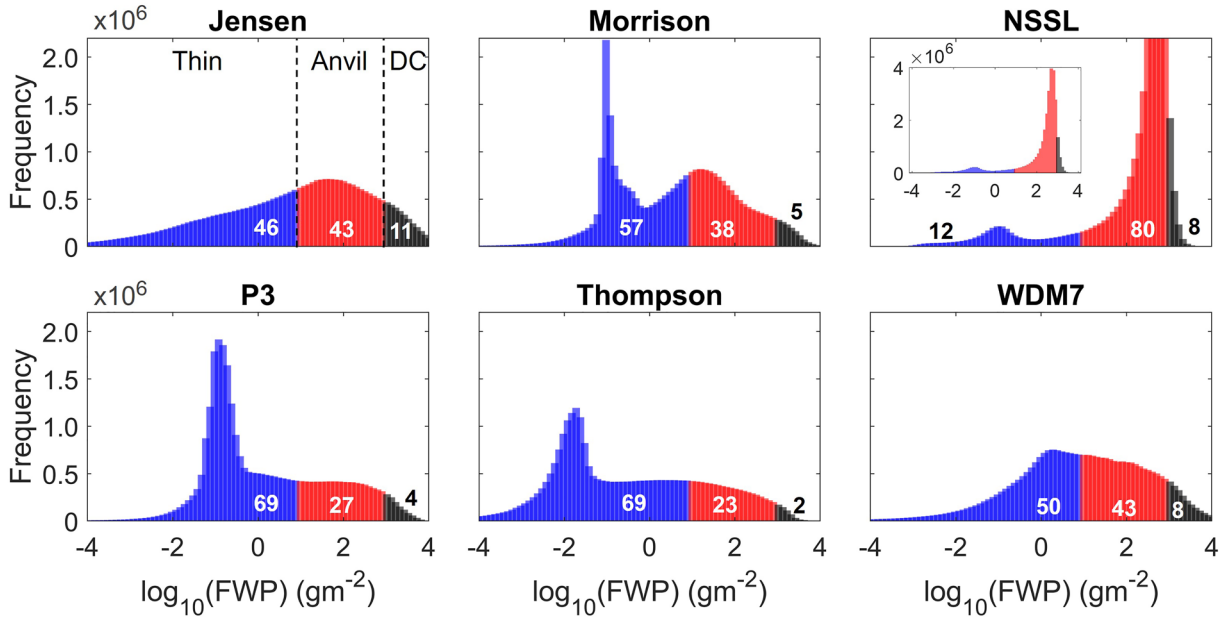

Figure 2. Frequency distribution of the total frozen water path (FWP, g m^{-2}), in base-10 logarithm, from $t = 4$ hr onward, during the 15-hr simulation. The gray filled bars represent the deep convective (DC) stage, the red represents the thick anvil stage, while the blue represents the thin cirrus stage. The overall percentage of grid of points corresponding to each stage is specified. The peak of the FWP distribution for the NSSL scheme exceeded the plot scale and is shown in the inset.

through to completion, Figures 2 and 3 illustrate the overarching differences in the development of deep convection. In later sections, we examine how the vertical distribution of frozen hydrometeors changes over time, along with their contribution to latent heating and consequently, updraft boosting.

3.1. Evolution of Frozen Hydrometeors

In the following figures, we dissect the overall storm evolution across the schemes in terms of variations in hydrometeor mixing ratios and their effect on heating and cooling rates. Pathways for frozen hydrometeor production/loss vary significantly across the schemes and their net effect can be seen in terms of the total frozen water content (Figure 4). The figure below shows the 99th percentile of frozen hydrometeor mixing ratio, calculated over the horizontal domain as a function of time and altitude (a similar representation of the liquid water content is shown in Figure S2 in Supporting Information S1). Across most schemes, frozen hydrometers initially formed $\sim t = 2$ hr and their mixing ratio increased significantly around $t = 5$ hr. The Thompson run was an exception: it produced larger frozen hydrometeor mixing ratios than other schemes during $t = 2$–5 hr, reaching altitudes up to 8 km but did not show a sustained increase in frozen water content thereafter. Frozen water mixing ratios near and at the tropopause were always below 1 ppm in the Thompson scheme. There were similarities between the overall trajectory of the Thompson run in this study and that in a recent 2-D squall line microphysics intercomparison effort (Bao et al., 2019): an early peak in hydrometeor production with weaker convection in later stages. Large frozen water content was observed in the Jensen scheme (see Movie S1 for a 3-D visualization), distributed relatively evenly over heights ranging 5–12 km (with a peak ~10–11 km) for $t > 7$ hr. The P3 and Morrison simulations show a qualitatively similar pattern but with lower frozen water contents, and over lower altitudes. The vertical distribution of frozen water content in the NSSL scheme was narrower than all other schemes; substantial frozen hydrometeor concentrations (>100 ppm) in the NSSL scheme only occurred between 6 and 8 km. The peak of the vertical distribution gradually shifted upwards over time. In the WDM7 scheme,

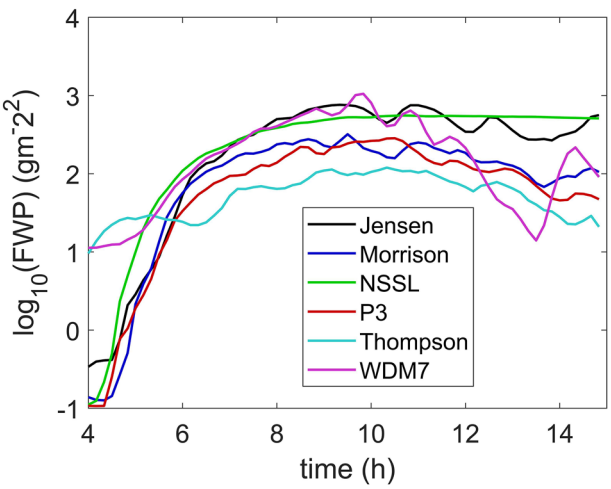

Figure 3. Time evolution of the domain-mean total frozen water path (FWP, g m^{-2}), in base-10 logarithm, from $t = 4$ hr onwards.

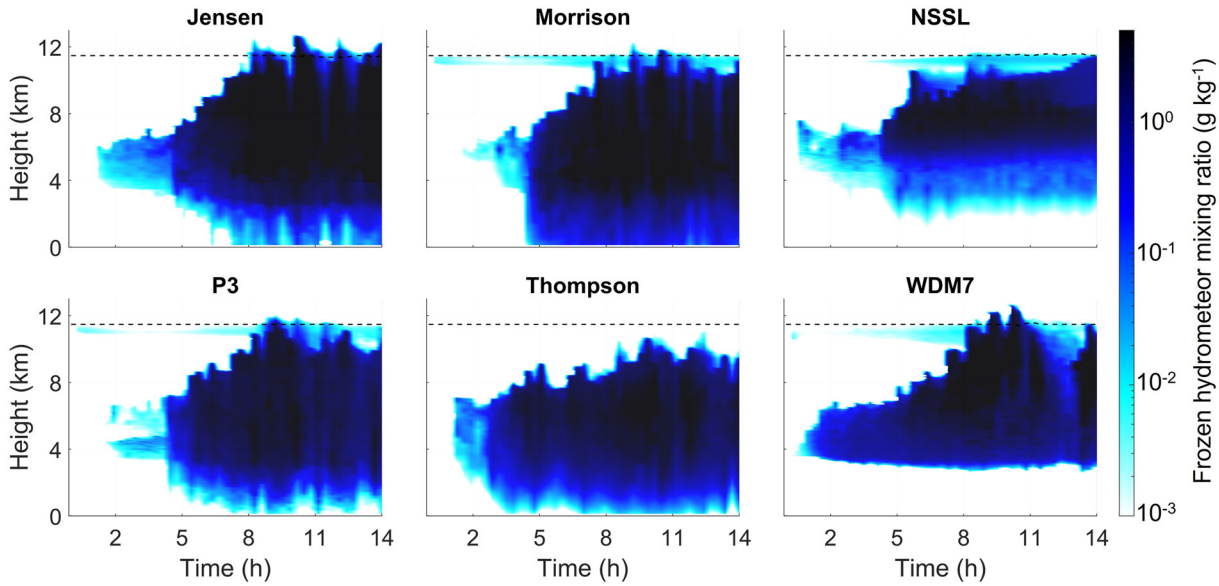

Figure 4. Time-height plots of the 99th percentile of frozen hydrometeor mixing ratio (g kg^{-1}) on a logarithmic scale, with a lower threshold of 1 ppm. The dashed black line indicates the tropopause level (~11.5 km). Cold-point tropopause level was estimated as the minima of domain (x–y) minimum all-sky temperatures. The freezing level for all runs was located ~3.8 km.

frozen hydrometeors reach a strong peak both in terms of magnitude and highest altitude between 9 and 11 hr and show a clear depletion around t = 12 hr, followed by a shallower increase at t = 14 hr. The frozen water distribution was centered high, ~8 km during most intense period, and no frozen hydrometeors were observed under ~3 km. Overall, there are similarities in the time evolution and altitude distribution of frozen hydrometeors in the Jensen, Morrison and P3 runs. The Thompson run shares some similarities with the above but showed an earlier initiation and lower peak altitudes. The NSSL and WDM7 runs produced markedly different hydrometeor distributions which were confined in a narrow altitude space.

Figures 5 and 6 highlight major differences in ice phase microphysics for these schemes, broken down by frozen hydrometeor types. Ice particle shape is prognosed only in Jensen microphysics, while most of the other schemes distinguish between ice species based on their size and density. For the current study, Jensen scheme indicates a dominant planar ice habit during the early stages of the storm, within the range of deep convection and thick anvil shown in Figure 4a. This figure shows a significant difference in the presence of different ice habits along the life cycle of the storm. At the onset of convection, the ice particles are predominantly planar with a small number of columnar shapes. In the mature stage, which is characterized by thick anvils, the contribution of columnar

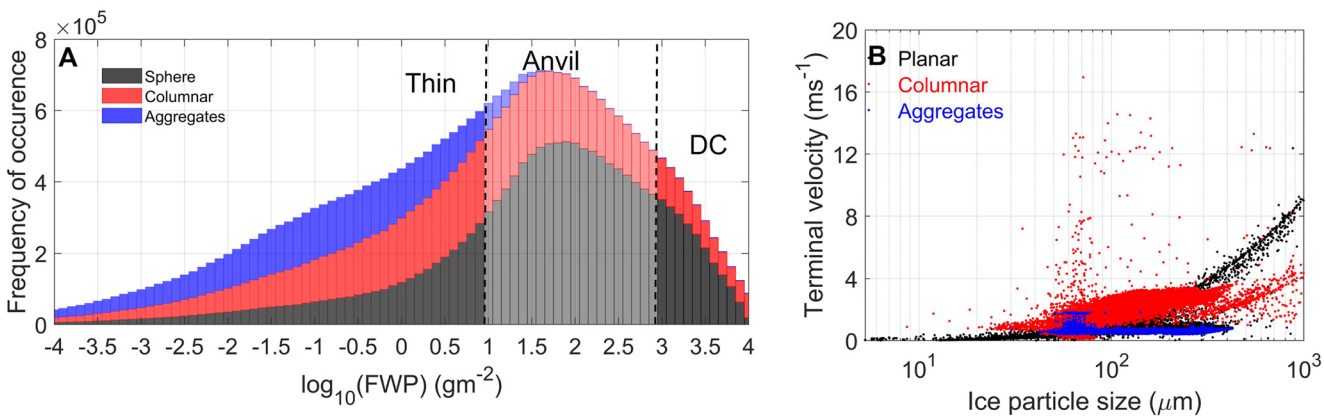

Figure 5. (a) Frequency distribution of the total frozen water path (FWP, g m^{-2}) same as in Figure 1, subdivided by ice habits (black: planar, red: columnar and blue: aggregates) in Jensen microphysics, and (b) Ice terminal velocity versus ice particle size for each habit.

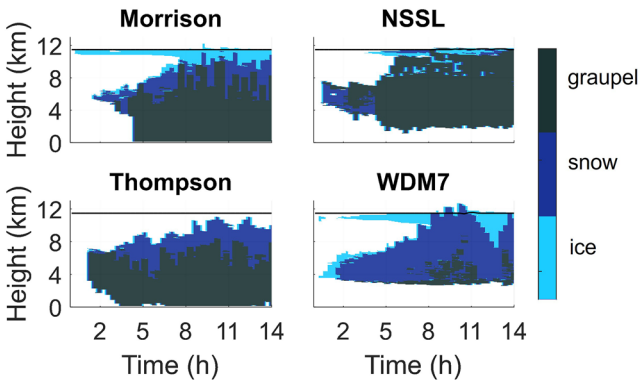

Figure 6. Time-height representation of dominant frozen hydrometeor species.

starts to increase slightly and particle aggregation begins to appear. Finally, in the last stage where the three forms are in competition, planar and columnar shapes gradually decrease, and aggregation dominates. A time-height representation of the ice-habit evolution (similar to Figure 6 below) is shown in Figure S3 in Supporting Information S1.

In the Jensen scheme, mass-weighted ice fall speeds are explicitly predicted for each ice habit, in contrast with other bulk schemes which calculate fall speed as a function of a maximum diameter. Figure 5b demonstrates the impact of ice habit on particle fall speeds, which in turn affects microphysical process rates. Higher terminal velocities favor sedimentation over sublimation and vice versa. For ice particles smaller than 20 μm, shape sensitivity is not significant. Beyond this threshold, the fall speed changes drastically depending on the shape of the ice particles. Planar ice particles smaller than 50 μm are associated with near-zero fall speed. These ice particles are likely to sublimate and contribute to diabatic cooling, while larger ice particles (>300 μm) are likely to sediment quickly. Ice aggregates, and a large fraction of columnar ice particles occupy an intermediate size range, where sublimation and sedimentation are modulated by supersaturation with respect to ice. However, because of the difference in ice particle density, aggregates have a smaller terminal velocity than columnar ice for a given particle size. Ice aggregates which are the dominant ice habit in optically thin cirrus persist at and above the tropopause, producing a radiative heat gradient (heating below and cooling above) which prolongs cirrus life cycle.

For the four schemes with predefined hydrometeor categories, Figure 6 shows the dominant hydrometeor type, in terms of contribution to the domain-averaged total frozen water content, as a function of altitude and time. As in Figure 4, this analysis was limited to regions with frozen water content greater than 1 ppm. Across these schemes, there are differences in ice-snow threshold sizes (Table 2), which follow the order: Morrison > WDM7 = NSSL > Thompson. Therefore, each hydrometeor category corresponds to a different particle size range in each of the schemes. Note that while conversion of hydrometeors from one category to another involves kinetic processes, and is not simply a function of cutoff size, the threshold sizes that separate ice and snow in these schemes are significant for determining how much cloud ice is allowed to grow before it can be converted to snow. This is associated with differences in the mixing ratio distributions of cloud ice and snow, as well as their size distributions. The mean effective radii of cloud ice in these schemes exhibited the following order: Thompson (10–30 μm) < NSSL ≈ WDM7 (30–50 μm) < Morrison (40–60 μm). As Thompson has much a smaller snow-ice threshold than other schemes, ice mixing ratios were lower and ice particles in that run were smaller than those in other runs. This is a likely cause of less intense latent heating, since there is less ice growth from deposition in the convective updrafts.

Further, formulations of hydrometeor density (see Table 2) and terminal velocities vary among the schemes. All of the schemes include many of the same production/reduction pathways for ice, snow and graupel. Ice is predominantly produced through nucleation, and homogenous freezing of cloud water, while ice reduction pathways include autoconversion to snow, as well as snow and graupel collecting ice. Snow is largely produced through autoconversion of ice, snow collecting cloud water and ice, and snow deposition. Snow reduction pathways include rain collecting snow, sublimation, and melting. Snow collecting rain and cloud water, and deposition are the major graupel production pathways and the main reduction pathways involve sedimentation, melting and

Table 2
Characteristic Ice/Snow Thresholds and Frozen Hydrometeor Densities for the Four Microphysics Schemes in Figure 6

	Morrison	NSSL	Thompson	WDM7
Ice/Snow threshold (μm)	650[a]	500[b]	150[a]	500[b]
Bulk particle density (kg m^{-3})	Ice–500	Ice-calculated	Ice–890	Ice-calculated
	Snow–100	Snow–100	Snow–100	Snow–100
	Graupel–400	Graupe-predicted (range: 300–900)	Graupel–500	Graupel–500

[a]upper bound in the intercept parameter of fall speed calculation. [b]maximum allowed size of cloud ice.

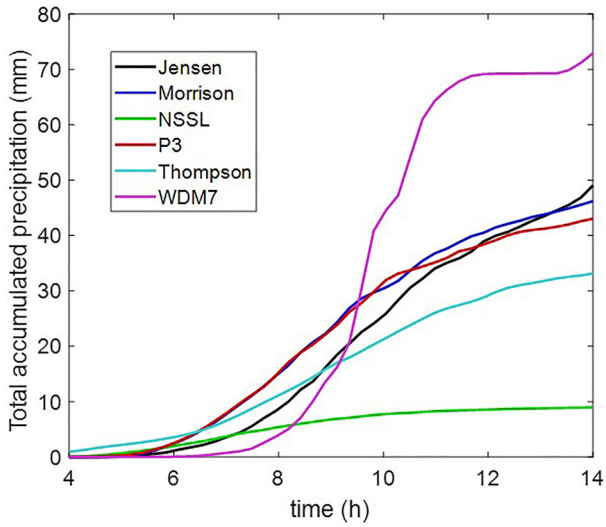

Figure 7. Total accumulated (grid-scale + cumulus) precipitation over time.

rain collecting graupel. The linkage between rates of dominant production/reduction processes for frozen hydrometeors and their size distributions are bi-directional: process rates are size-dependent and production/reduction processes, in turn, affect the size distributions. Also, as is clear from the process terms described above, production/reduction of rates of different hydrometeor categories are inter-dependent.

Additionally some of the scheme include certain less common pathways; the total number of pathways are too numerous—10 to 20 per schemes—to fully discuss here. However, even for the same pathways, formulating equations and parameters may differ and even for identical formulations, the schemes can produce varying behavior due to the size-dependence of these process terms. In an intercomparison of a subset of schemes evaluated here (Morrison, Thompson and WSM6—a scheme very similar to WDM7), Bao et al. (2019) documented large disparities in the properties and process-level behavior of hydrometeor categories. These differences in categorization limit the value of comparing hydrometeor categories across schemes.

However, the simplified representation in Figure 6 is still useful for examining the evolution of frozen hydrometeors within each microphysical setup. In the Morrison simulation, there is an apparent size sorting effect where cloud ice dominates at the highest altitudes, near and at the cold point tropopause (CPT), followed by snow and then graupel. The frozen hydrometeor mass in the Thompson scheme is dominated by snow for altitudes greater than ~6 km and by graupel below that. As specified in Table 2, This scheme uses a relatively low radius threshold of 150 μm, above which frozen particles are considered large enough to be classified as snow (Bao et al., 2016). The NSSL scheme resulted predominantly in graupel formation, and only small "pockets" of mixed ice and snow. These graupel particles, unlike those in other schemes, remain aloft up to 10 km. This is likely due to the fact that the NSSL scheme predicts average graupel particle density (Mansell et al., 2010), and allows for low-density (therefore, low terminal velocity) graupel. Further, in a recent update to this scheme, the fall speed calculation from Ferrier (1994) was adopted, which results in lower fall speeds (Mansell & Ziegler, 2013). In the WDM7 scheme, ice is initially formed at and below the tropopause, which grows in strong updrafts (see Figure 11) and drives snow production through autoconversion when a threshold size of 500 μm is reached.

In general, snow and graupel are more likely to precipitate, making them important moisture sinks. The time evolution of the simulated dominant size of snow and graupel particles is an important determinant of the onset of precipitation and its contribution to evaporative cooling. Similar to Bao et al. (2019), we find that precipitation (Figure 7) begins quicker in Thompson than in other schemes—an indication of larger graupel size—but the quick removal of graupel implies that precipitation is slowed until snow particles grow large enough to precipitate (see $t = 5$–7 hr in Figure 6). In the NSSL scheme, graupel particles largely stay aloft above the freezing level, and the precipitation in this scheme is much smaller than all other schemes. In WDM7 scheme, significant graupel production is observed around $t = 8$ hr, along with the onset of large amounts of precipitation. Jensen, Morrison and P3 schemes show comparable amounts of precipitation.

Precipitation interacts with storm energetics by contributing to evaporative cooling, which intensifies the storm. There are several other mechanisms through which differences in hydrometeor loading and properties produce variability in storm energetics (Section 3.3), and the UTLS hydration observed at the end of the simulation period (Section 4). However, prior to furthering the comparisons between these schemes, we describe the supplemental 2-D simulation (Section 3.2) that was performed to evaluate the dependence on simulated storm characteristics on domain size.

3.2. Large Domain 2-D Simulation

A 3-D large domain (200 × 200 × 30 km) model configuration, with grid spacing smaller than 200 m is beyond our available computational resources. To circumvent these limitations, we opted to run a 15-hr large-domain (200 km × 30 km) 2-D simulation with Jensen microphysics. The objective of this simulation was to determine whether changing the domain size results in a significant difference in (a) the vertical structure of the storm

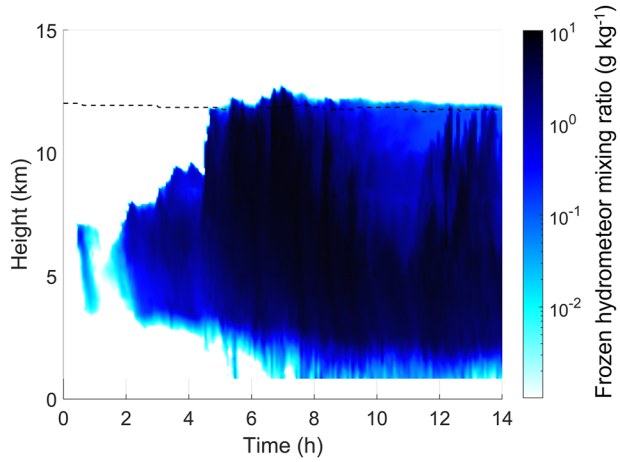

Figure 8. Time-height plots of the 99th percentile of frozen hydrometeor mixing ratio (g kg^{-1}) on a logarithmic scale. The dashed black line indicates the tropopause level (~11.5 km).

and/or (b) the timing of storm initiation and dissipation. For the 2-D simulation, except for the grid spacing, all other model configuration details are identical to the 3-D simulation with Jensen scheme. The results (Figures 8 and 9) are broadly consistent with those from the small domain in 3-D simulation. The storm peak (as seen in the ice mixing ratio and updraft plots) occurs earlier (~t = 7 hr) but these differences are to be expected with the change in dimensionality and horizontal resolution. In the 2-D simulation, there is a significant weakening of the storm around t = 10 hr but around there was a resurgence at t = 12 hr, in terms of the frozen hydrometeor loading near the tropopause level, as well as renewed updrafts (Figure 9) are observed. In comparison, in the small-domain 3-D simulation (Figure 4 of this manuscript), no such sustained weakening is observed. The associated UTLS hydration in the large-domain ranges 50–70 ppmv, which is lower than moisture values (~100 ppmv) obtained from the small-domain simulation. However, this difference is much smaller than the variability across different microphysics schemes (discussed in Section 3.4). These findings indicate that while domain size affects the simulated convective strength, there is consistency between the small and large domains in terms of how convection is represented. Therefore, we do not expect domain size to be a confounding factor in the interpretation of our findings about the relative performance of the different microphysical schemes.

3.3. Latent and Radiative Heating and In-Cloud Motions

Microphysical parameterizations modulate storm dynamics through their contribution to energetics. Ice microphysical properties (such as size, shape, density) affect cloud lifetime, both through their direct effect on fall speed and through their interaction with latent heating and radiative effects. Therefore, varying treatments of hydrometeor types and associated size distributions and densities leads to differences in simulated storm energetics. Latent heating is a first-order determinant of vertical motions, which in turn affect hydrometeor evolution.

To investigate the contribution of parameterized microphysical processes to vertical fluxes, we explore the diabatic heating from microphysics across the six schemes. We use outgoing longwave radiation (OLR) as a proxy for the radial distance outward from the core of deep convection with lower OLR values occurring closer to the core. Figure 10 shows latent heating in the OLR-height space, averaged between t = 9–12 hr, within 20 OLR bins evenly spaced between 115 and 275 Wm^{-2}. Histograms of the OLR distribution for those intervals are overlaid. The chosen coordinates allow for a convenient assessment of the strength of deep convection across schemes. The comparison reveals a large spread in the vertical and horizontal organization of energy growth/depletion in clouds. Two of the schemes—Thompson and NSSL—exhibit stronger latent heating at higher OLRs than all other schemes and have no domain points within the lowest OLR bin. The NSSL scheme is also associated with higher latent heating for altitudes ranging 4–6 km, indicating hydrometeors formation/growth primarily at lower altitudes. The associated low-level horizontally homogeneous convection hampers the formation of deep convective clouds and prevents convection from reaching high altitudes. The remaining schemes show stronger aggregation, with large latent heat release in the lowest OLR bins, indicating hydrometeor growth within the core of deep convection. The gradient in latent heating, moving outward from the convective core is associated with circulation patterns that enhance buoyancy. (e.g., Labbouz et al., 2018). The Jensen, Morrison and P3 runs showed a bimodal distribution of latent heating in the OLR-height space. One peak of the distribution is located in the lowest OLR bin (the convective core) over a broad vertical range extending from ~4 km to ~10 km. The second peak is spread over a range of higher OLR values and located at low altitudes (2–3 km). These peaks are separated by a mid OLR region of net-zero or negative latent heating. In the WDM7 run, on the other

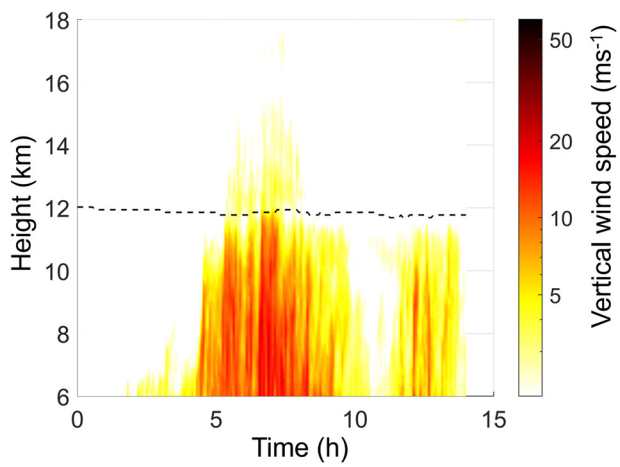

Figure 9. Time-height plots of the 99th percentile of vertical wind velocity (ms^{-1}) on a logarithmic scale. The lower limit on the color axis is 1 ms^{-1}. The dashed black line indicates the tropopause level (~11.5 km).

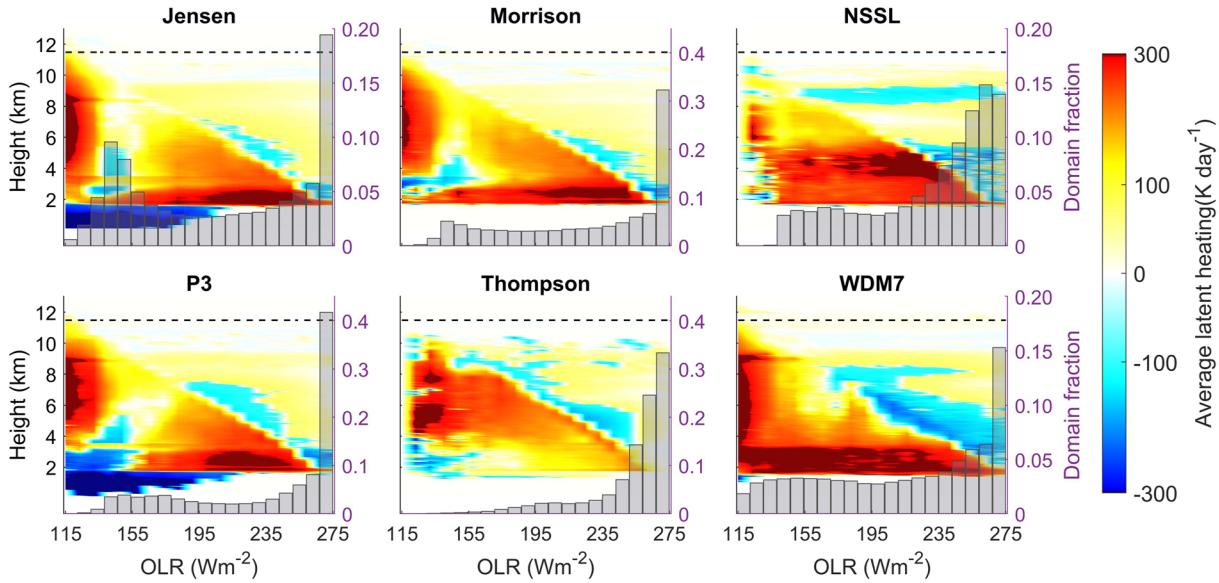

Figure 10. Vertical variation in latent heating (K day^{-1}) averaged within each of 20 outgoing longwave radiation (OLR, Wm^{-2}) bins between t = 9–12 hr. The overlaid histograms (corresponding to the y-axes on the right) shows the fraction of the domain occupied by the each OLR bin. The dashed black line represents the cold-point tropopause level.

hand, the two peaks are merged, with no separating region. Jensen and WDM7 have significant fractions of the domain associated with low OLR values (overlaid histograms). Note that scale of the histograms (right y-axes) for the Jensen and WDM7 schemes is different from that for the Morrison and P3 schemes. There is a peak in the OLR distribution for the Jensen scheme at ∼140–150 Wm^{-2}, while the distribution for WDM7 is nearly uniform. A further difference between the two schemes is the larger latent heating at lower levels in WDM7, associated with snow and graupel formation and growth, as shown in Figure 6. Finally, there is strong cooling in the Jensen

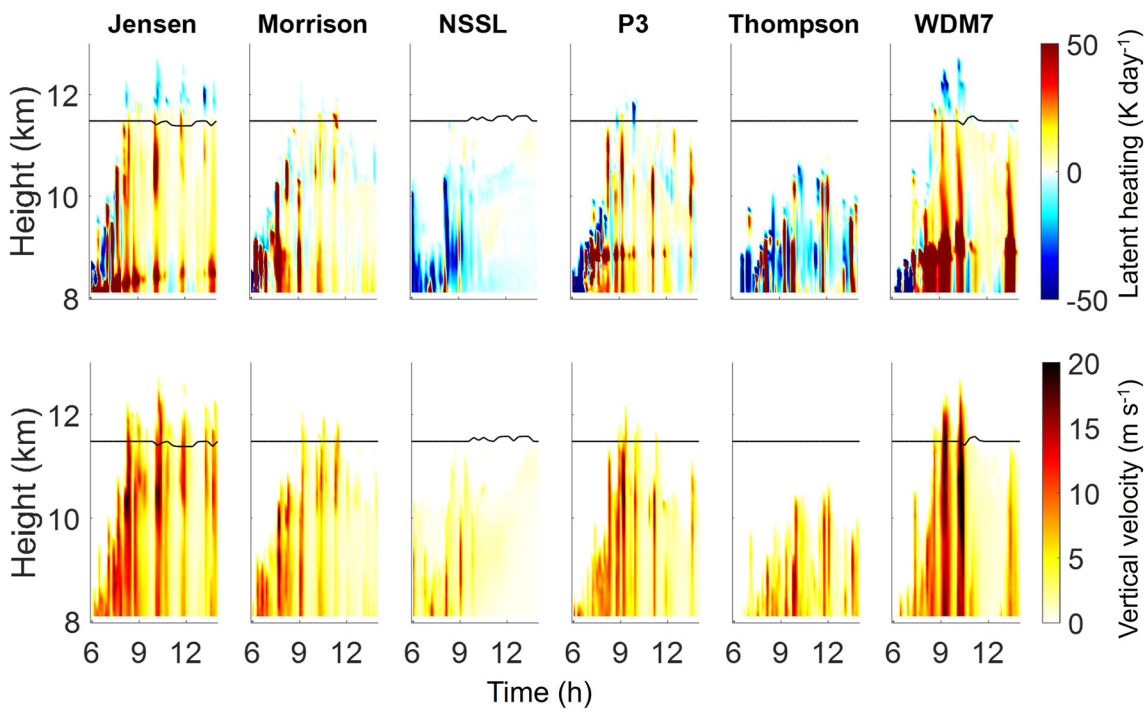

Figure 11. Time-height plots of (top panels) domain-averaged in-cloud latent heating tendency (K day^{-1}) and (bottom panels) the 99th percentile of in-cloud vertical velocities (m s^{-1}). The black line represents the tropopause level.

and P3 schemes in the 9–12 hr period, but weak or no cooling in the sub-4 km altitude range in other schemes. Overall, Figure 10 provides a summary of the impact of microphysics on the horizontal and the vertical extent of convective clouds, with the caveat that the interaction between vertical motion and microphysics occurs in both directions.

The links between microphysics and latent and radiative heating are crucial in determining the longevity and vertical extent of convective clouds. Latent heat release in updrafts primarily drives a deep circulation pattern in the early stage of a convective storm (Gasparini et al., 2019). Various phase-change microphysical processes such as evaporation/condensation, vapor sublimation/deposition and melting, are involved in modulating latent heating rates and the evolution of the thermodynamic profiles (Grim et al., 2009). Fan et al. (2017) have previously shown large variations in updraft velocities between different microphysical schemes, largely due to differences in latent heating. Several of the schemes in this work were also included in their study, and the observed trend in updraft strength was: Morrison > P3 > Thompson > NSSL (Fan et al., 2017). We also observe that updraft velocities in our simulations are driven by thermal buoyancy and therefore correlated with the latent heating patterns. Figure 11 shows the evolution of domain-average in-cloud latent heating rates (top panel) and time-height plots of the 99th percentile vertical velocities (bottom panels). For $t < 8$ hr, heating/cooling is confined to low altitudes, which is mainly due to liquid phase condensation. This is associated with development of updrafts reaching 9–10 km. For $t > 8$ hr, frozen hydrometeors start contributing significantly to diabatic heating/cooling. The Jensen, Morrison, P3 and WDM7 schemes broadly show a similar evolution, with alternate heating and cooling periods over time, but the intensity varies across the schemes. Strong latent heating corresponds to the presence of strong convective updrafts: water vapor condenses as warm air rises and latent heat is released into the atmosphere, further boosting the vertical velocities. In the dry environment above the tropopause, hydrometeors are subject to evaporative cooling. The density and terminal velocity distribution of hydrometeors is an important factor in determining sedimentation and therefore, the altitudes over which evaporative cooling occurs.

Between 8 and 10 hr, the largest heating was observed for the WDM7 scheme, followed by the Jensen scheme. In the WDM7 run, water vapor transported by strong updrafts led to the formation of more mixed phase hydrometeors, and thus strong heating persisted till $t \sim 10$ hr. This was associated with evaporating rain (not shown) that cooled the atmosphere below the freezing level. Due to the saturation adjustment imposed in WDM7, which involves abrupt removal of condensate via precipitation when supersaturation is reached, the nucleation of new ice particles and growth of ice particles are both inhibited, especially at the cold-point tropopause level. Once the supersaturation threshold is reached ($t \sim 10$ hr), only sublimation and sedimentation are possible, leading to significant cooling at and beyond the tropopause level. The Thompson scheme did not show a pattern of strong heating above 10 km, while almost all latent heating in NSSL occurred, below the altitudes of interest. High cooling rates are observed at around $t = 6$ hr in both cases, which hampers further development of convection. In the Thompson run, snow is produced in the early stages of convection and converted to large graupel particles that sediment in the first 6 hr. This low-level sedimentation depletes liquid water from the entrainment zone and limits the strengthening of evaporative cooling entrainment leading to weak and homogeneous convection throughout the whole domain (Bretherton et al., 2007; de Lozar and Mellado, 2015). This is also apparent in the absence of a low-OLR peak in latent heating in NSSL and Thompson in Figure 10 above. Previous studies (Adams-Selin et al., 2013a, 2013b; Bao et al., 2016) have highlighted the importance of graupel particle size in cold-pool development and storm-intensification following the initiation of convection: large and/or heavy graupel particles produced in the early stages of a storm simulation correspond to weaker convection in the mature stage. In the NSSL run, graupel particles dominate the frozen hydrometeor mass after $t = 5$ hr and extend up to ~10 km. Evidently, these are particles with lower fall speeds than those in the Thompson or Morrison runs and can therefore, contribute to evaporative cooling at higher altitudes. Thus, parameterizations of particle density and fall speed affect storm energetics and therefore, the strength of deep convection. Figure 11 indicates that, on average, sublimation cooling controls the latent heat profile between 8 and 10 km, with heating processes (such as deposition and raindrop-freezing) largely occurring at lower altitudes in the NSSL and Thompson runs.

To the first order, latent heating controls updrafts and boosts/inhibits hydrometeor formation and growth. However, radiative heating is an important factor in the evolution of cloud structure and provides insights into the some of the subtler differences between the runs.The evolution of mean in-cloud radiative heating tendency is shown in Figure 12. Cloud-radiation interactions are a function of optical thickness and effective cloud particle size. In general, clouds, of a given optical depth, composed of larger particles absorb less longwave radiation and exert less cloud infrared radiative forcing (Fu et al., 1995). Clouds with intermediate optical thickness ("modal"

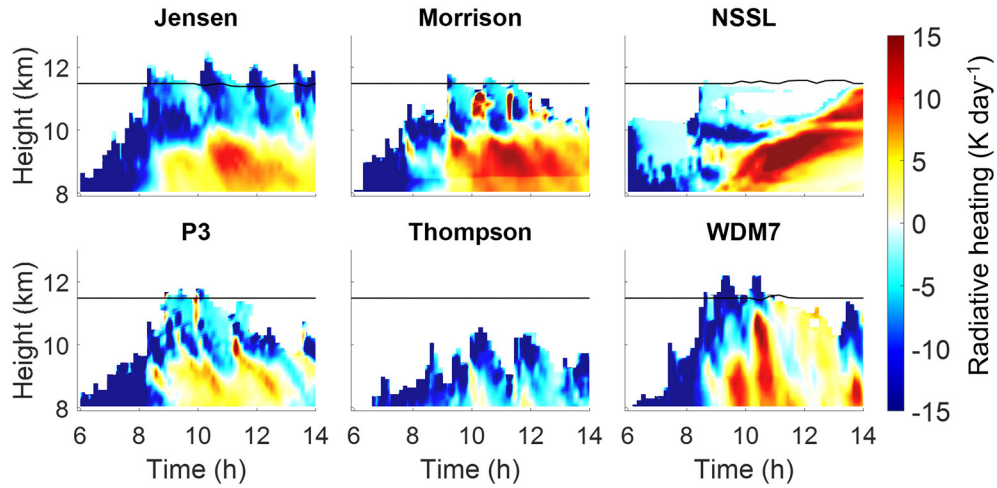

Figure 12. Time-height plots of domain-averaged in-cloud radiative heating tendency (K day^{-1}). The black line represents the tropopause level.

anvils in Sokol and Hartmann (2020)) are associated with strong heating near the base and cooling at the top, which destabilizes the atmosphere and promotes convection (Fu et al., 1995; Hartmann & Berry, 2017; Schmidt & Garrett, 2013). Thin cirrus clouds are heated throughout, which gradually lofts them across isentropic surfaces but also causes relatively rapid lateral spreading (Dinh et al., 2010; Schmidt & Garrett, 2013). The net result is that the isentropic surfaces stay approximately flat. Clouds with very high optical thickness, especially those with high bases, experience very strong heating, causing them to evaporate and/or rise rapidly (Hartmann & Berry, 2017). This was the case with the NSSL run, which had a very large mode of frozen water path (Figure 2) and showed evidence of evaporation (negative latent heating in Figure 11) as well as a rising cloud base (Figures 4 and 11). The Jensen, P3 and WDM7 results showed a destabilizing heating dipole pattern: vertical transition from heating to cooling at altitudes ranging from 9 to 11 km. The Morrison run was characterized by a similar pattern but periodically, strong radiative heating (>4 K day^{-1}) was observed near the cloud tops. As shown in Figure 4, the distribution of frozen hydrometeors for these runs broadens over time in the altitude space and therefore, radiative heating occurs at lower vertical levels. This leads to tilted structure observed in radiative heating for these schemes. In the Thompson run, the cloud base is optically thinner and lower than in the other schemes, which is reflected in the radiative tendency: a significantly weaker radiative heating dipole is observed than in the other schemes (with the exception of NSSL which did not produce a clear dipole structure). The strength of the heating dipoles is linked to upper-level cloud circulation and therefore, cloud horizontal motions (Gasparini et al., 2019).

In addition to the vertical structure of radiative heating, horizontal gradients in radiative tendencies (within clouds and the differences between cloudy and clear-sky regions) can modify anvil clouds by driving a mesoscale circulation (Wall et al., 2020). This results in lifting and spreading of anvils (like the mechanism described for thin cirrus above) and enhances their longevity by offsetting gravitational settling of large cloud particles. In Figure 13, we use the range of radiative heating/cooling values (difference between the 99th and 1st percentiles) as measures of horizontal gradients. For schemes other than Thompson, the strongest horizontal gradients in radiative heating are around 10 km. In the NSSL simulation, radiative gradients emerge strongly at 8 km, around $t = 9$ hr and thereafter spread up to 10 km altitude. Jensen and WDM7 exhibit differential radiative heating around the tropopause. A key difference between these schemes is that strong tropopause level radiative heating gradients occurs earlier in the WDM7 run than in Jensen. Figure 12 showed a similar difference between the schemes in terms of the vertical heating dipole structure. The bottom panels of Figure 13 show that cloud horizontal velocities (root-mean-square of the two horizontal components) are linked with radiative heating gradients, and high horizontal velocities are observed earlier and at higher altitudes in WDM7 than in Jensen. Thus, there is stronger horizontal thinning of clouds at high altitudes between $t = 8$–10 hr in the WDM7 run, which likely contributes to the weakened convection at these altitudes after a fraction of the hydrometeors is removed due to saturation adjustment. As in other outputs of interest, radiative heating gradients and horizontal motions in the Morrison and P3 runs were qualitatively similar to, but weaker than those in the Jensen run.

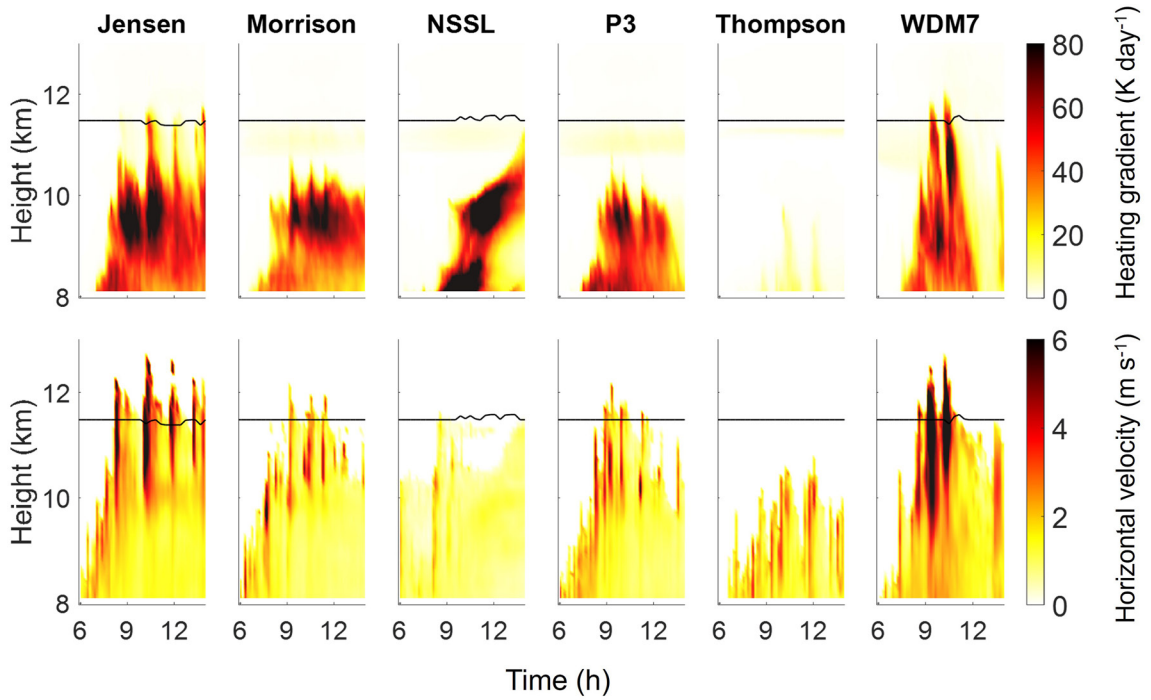

Figure 13. Time-height plots of (top panels) horizontal range in radiative heating tendency (K day^{-1}) and (bottom panels) the 99th percentile of cloud horizontal root-mean-square velocities (m s^{-1}). The black line represents the tropopause level.

3.4. UTLS Hydration

The evolution of the vertical distribution of water vapor is shown in Figure 14. For reference, aircraft observations for the supercell convective storm observed over central Oklahoma during the DC3 campaign indicate vapor concentrations ranging 100–200 ppmv at the tropopause (Phoenix et al., 2017). At the tropopause level, only the Jensen run yields maximum water vapor concentrations >100 ppmv for all t > 10 hr. In the WDM7 run, we observe strong hydration at t = 10 hr (corresponding with the strong updraft in Figure 11) followed by dehydration to ~50 ppmv. Water vapor transport to altitudes above the CPT was significant in the Jensen, WDM7 and P3 simulations, corresponding to increases at 12 km in the maximum mixing ratio (relative to a 0–4 hr baseline) of 110, 70 and 60 ppmv, respectively. Hydration above the tropopause was strongly linked to the strength

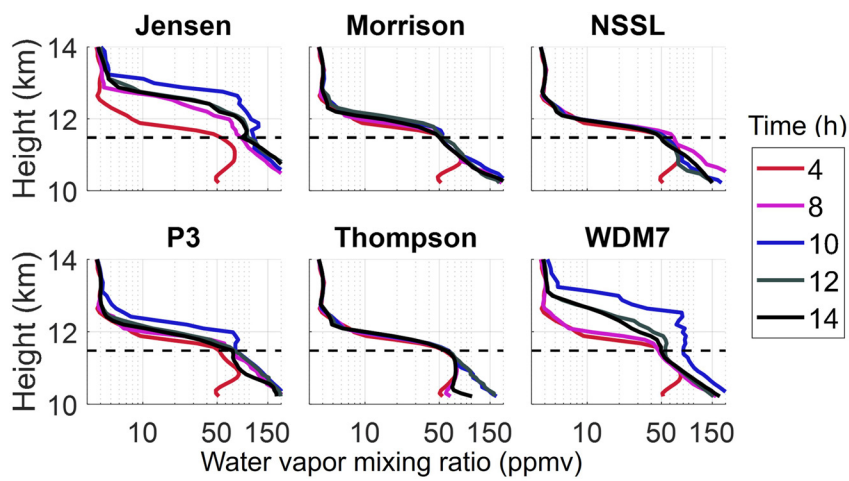

Figure 14. Vertical profiles of domain maximum water vapor mixing ratios for selected times. The dashed black line represents the average tropopause level over this period.

of tropopause penetrating updrafts (Figure 11). The Morrison, NSSL and Thompson runs (in decreasing order) showed much smaller increases (8–25 ppmv) in the water vapor mixing ratio just above the tropopause level. All schemes show comparable evidence of hydration below the tropopause (10–11 km), but in the Thompson run UT hydration peaked between 10 and 12 hr and declined by the end of the simulation period. For all schemes, maximum UTLS hydration (change in water vapor mixing ratios, relative to the 0–4 hr averaged baseline), occurs above the tropopause at altitudes ranging 12–12.5 km, between t = 10–12 hr. We quantify the relative LS hydration as percentage change in the 99th percentile of water vapor mixing ratio. Maximum LS hydration was ∼400% for Jensen and WDM7, 130% for P3, 100% for Morrison, 55% for NSSL and 40% for Thompson.

We estimated the direct water vapor transport (at a specified vertical level) as:

$$q_{v,\mathrm{flux}} = \sum_{n_t=1}^{T} \sum_{n_s=1}^{S} \delta s \delta t w(x, y, t) q_v(x, y, t) \tag{1}$$

where T and S are the total number of time steps and horizontal grid boxes, respectively, and δt is the time step, δs is the grid surface area, w is the vertical wind speed, q_v is the water vapor mixing ratio.

We also calculated the contribution of microphysics to LS hydration, using the water vapor microphysical tendencies from WRF output. At the level of maximum hydration (discussed above), the contribution from microphysics (sublimation/deposition) to net hydration is negligible (<1%) for all schemes other than Jensen and WDM7, consistent with the relatively low frozen hydrometeor loadings observed for those schemes (Figure 4). For Jensen and WDM7, 95%–96% of the hydration is attributed to direct transport of vapor. In their deep convection case study, Qu et al. (2020) noted that the relative significance of hydration mechanisms varied significantly with grid size: direct water vapor transport contributed 40% of the total hydration in a 2.5 km grid simulation but 89% to that in a 1 km grid simulation. This was attributed to stronger vertical advection in the 1 km simulation, which in turn was linked with more turbulent wave-breaking activity. The higher spatial resolution in this study is expected to better resolve updrafts and is likely to be associated with greater turbulent mixing than the 1 km simulation in Qu et al. (2020).

4. Conclusions

This study was designed to examine the effect of microphysics parameterizations, isolated from any other factors, on the evolution of a deep convective storm and the associated hydration above the cold-point tropopause level. Six bulk microphysics schemes—representing the diversity in prevailing approaches to microphysical parameterization—were tested in otherwise identical high-resolution setups. We used WRF-LES initialized with a sounding profile representative of a tropopause-overshooting storm observed over central Oklahoma on May 19th −20th 2012, as part of the Deep Convective Clouds & Chemistry Experiment (DC3) campaign. Model experiments were designed to observe the effects of microphysics, without confounding effects from insufficient resolution, and document their contribution to the variability in key characteristics of a deep convective storm.

All schemes produced the highest reaching updrafts 8–12 hr into the simulation and the largest hydration above the tropopause occurred at t = 10 hr. Varying microphysics produced large differences in the strength and vertical extent of convection. Variations in hydrometeor size-dependent microphysical processes among the schemes led to differences in vertical profiles of direct-microphysical (latent) heating and their evolution in time. This was associated with significant differences in updraft strengths, particularly at and above the CPT. The schemes tested here varied widely in the highest vertical levels at which latent heating dominates (with evaporative cooling at higher altitudes), which is evidence of underlying differences in density and terminal velocity distributions of hydrometeors. We also observed differences in radiative heating profiles, as well as their horizontal gradients, which potentially affects in-cloud circulations. Finally, these schemes exhibit varying degrees of convective aggregation. In schemes with weaker connection, horizontally homogeneous hydrometeor formation and growth at lower altitudes hampers the formation of deep convective clouds and prevents convection from reaching high altitudes.

The two schemes—Thompson and NSSL—that produced the weakest convection operate at different levels of complexity but in both, the frozen hydrometeor content skewed heavily toward graupel. Graupel particles in the Thompson run began settling early in the simulation period, thus removing moisture. In contrast, light graupel in

the NSSL run extended to high altitudes and contributed to evaporative cooling in the upper tropopause. In both cases, there was too little latent heating to boost the updrafts in the 10–12 km altitude range. Further, the NSSL run exhibited very strong cloud radiative heating with weaker cooling at cloud tops, which can lead to evaporative dissipation of clouds. Notably, in a real case study of the storm that we aimed to simulate here, Phoenix et al. (2017) found that the NSSL scheme performed well in terms of model-observation comparisons. However, the idealized setup in this work precludes a direct comparison. The differences in horizontal resolution (100 m in this study vs. 2 km in Phoenix et al. (2017)) are also likely to produce differences in updraft strength and hydrometeor distributions (Dauhut et al., 2014; Qu et al., 2020).

The Jensen and WDM7 runs showed the strongest updrafts as well as horizontal circulations. However, a supersaturation threshold in WDM7 causes an abrupt shift to latent cooling following the strongest updraft. We found an order of magnitude variation in the amount of stratospheric hydration produced by these schemesSchemes with greater degrees of freedom (Morrison, NSSL, Thompson) do not generally produce deeper/more persistent convection that simpler schemes (WDM7) and may require case-specific tuning.

The numerous differences between the two-moment schemes, in category definition and associated process terms reflect real uncertainties and gaps in knowledge. Bao et al. (2019) provided a comprehensive overview of process-level differences between three schemes (Morrison, Thompson and WSM6) and provided a useful framework for microphysics evaluation. They suggested that observational data on hydrometeor size distributions can aid improvements in microphysical parameterizations. However, it should be noted that for two-moment schemes with several artificial hydrometeor demarcations, input parameters cannot be uniquely constrained by observations. Therefore, "particle property" schemes like P3 and Jensen comprise a promising development. Further high-resolution case studies of various types of convective storms using these schemes can help establish whether they are broadly suited for modeling convection. We emphasize the importance of evaluating diabatic and radiative heating profiles as a link between microphysics and convective lifecycle and intensity, and therefore, UTLS hydration.

Data Availability Statement

The sounding used to initialize the WRF model was obtained from the ARM archive. These data were from the Balloon-Borne Sounding System (SONDEWNPN), Southern Great Plains (SGP) Central Facility, Lamont OK (C1). Compiled by Keeler and Burke (2001).

A subset of the processed output files, that was used to generate the figures in this manuscript is archived at Pandey (2023).

Acknowledgments

This work was supported by the NASA Earth Venture Suborbital Dynamics and Chemistry of the Summer Stratosphere (DCOTSS) Grant 17-EVS3-17_10017. Z.K and F.L acknowledge the funding from NSF Grant 1743753. Computing and storage resources of the Harvard University research cluster were used for model runs and data analysis.

References

Adams-Selin, R. D., van den Heever, S. C., & Johnson, R. H. (2013a). Impact of graupel parameterization schemes on idealized bow echo simulations. *Monthly Weather Review*, *141*(4), 1241–1262. https://doi.org/10.1175/mwr-d-12-00064.1

Adams-Selin, R. D., van den Heever, S. C., & Johnson, R. H. (2013b). Sensitivity of bow-echo simulation to microphysical parameterizations. *Weather and Forecasting*, *28*(5), 1188–1209. https://doi.org/10.1175/waf-d-12-00108.1

Anderson, J. G., Weisenstein, D. K., Bowman, K. P., Homeyer, C. R., Smith, J. B., Wilmouth, D. M., et al. (2017). Stratospheric ozone over the United States in summer linked to observations of convection and temperature via chlorine and bromine catalysis. *Proceedings of the National Academy of Sciences of the USA*, *114*(25), E4905–E4913. https://doi.org/10.1073/pnas.1619318114

Anderson, J. G., Wilmouth, D. M., Smith, J. B., & Sayres, D. S. (2012). UV dosage levels in summer: Increased risk of ozone loss from convectively injected water vapor. *Science*, *337*(6096), 835–839. https://doi.org/10.1126/science.1222978

Bae, S. Y., Hong, S.-Y., & Tao, W.-K. (2019). Development of a single-moment cloud microphysics scheme with prognostic hail for the Weather Research and Forecasting (WRF) model. *Asia-Pacific Journal of Atmospheric Sciences*, *55*(2), 233–245. https://doi.org/10.1007/s13143-018-0066-3

Banerjee, A., Chiodo, G., Previdi, M., Ponater, M., Conley, A. J., & Polvani, L. M. (2019). Stratospheric water vapor: An important climate feedback. *Climate Dynamics*, *53*(3), 1697–1710. https://doi.org/10.1007/s00382-019-04721-4

Bao, J.-W., Michelson, S., & Grell, E. (2016). Pathways to the production of precipitating hydrometeors and tropical cyclone development. *Monthly Weather Review*, *144*(6), 2395–2420. https://doi.org/10.1175/mwr-d-15-0363.1

Bao, J. W., Michelson, S. A., & Grell, E. D. (2019). Microphysical process comparison of three microphysics parameterization schemes in the WRF model for an idealized squall-line case study. *Monthly Weather Review*, *147*(9), 3093–3120. https://doi.org/10.1175/mwr-d-18-0249.1

Barth, M. C., Cantrell, C. A., Brune, W. H., Rutledge, S. A., Crawford, J. H., Huntrieser, H., et al. (2015). The deep convective clouds and chemistry (DC3) field campaign. *Bulletin of the American Meteorological Society*, *96*(8), 1281–1309. https://doi.org/10.1175/bams-d-13-00290.1

Bretherton, C., Blossey, P. N., & Uchida, J. (2007). Cloud droplet sedimentation, entrainment efficiency, and subtropical stratocumulus albedo. *Geophysical Research Letters*, *34*(3), L03813. https://doi.org/10.1029/2006gl027648

Bryan, G. H., & Morrison, H. (2012). Sensitivity of a simulated squall line to horizontal resolution and parameterization of microphysics. *Monthly Weather Review*, *140*(1), 202–225. https://doi.org/10.1175/mwr-d-11-00046.1

Dauhut, T., Chaboureau, J. P., Escobar, J., & Mascart, P. (2014). Large-eddy simulations of Hector the convector making the stratosphere wetter. *Atmospheric Science Letters*, *16*(2), 135–140. https://doi.org/10.1002/asl2.534

Dauhut, T., Chaboureau, J.-P., Haynes, P. H., & Lane, T. P. (2018). The mechanisms leading to a stratospheric hydration by overshooting convection. *Journal of the Atmospheric Sciences*, *75*(12), 4383–4398. https://doi.org/10.1175/jas-d-18-0176.1

de Lozar, A., & Mellado, J. P. (2015). Mixing driven by radiative and evaporative cooling at the stratocumulus top. *Journal of the Atmospheric Sciences*, *72*(12), 4681–4700. https://doi.org/10.1175/jas-d-15-0087.1

Dessler, A. E., Schoeberl, M. R., Wang, T., Davis, S. M., & Rosenlof, K. H. (2013). Stratospheric water vapor feedback. *Proceedings of the National Academy of Sciences of the USA*, *110*(45), 18087–18091. https://doi.org/10.1073/pnas.1310344110

Dinh, T. P., Durran, D., & Ackerman, T. (2010). Maintenance of tropical tropopause layer cirrus. *Journal of Geophysical Research*, *115*(D2), D02104. https://doi.org/10.1029/2009jd012735

Fan, J., Han, B., Varble, A., Morrison, H., North, K., Kollias, P., et al. (2017). Cloud-resolving model intercomparison of an MC3E squall line case: Part I—Convective updrafts. *Journal of Geophysical Research: Atmospheres*, *122*(17), 9351–9378. https://doi.org/10.1002/2017jd026622

Ferrier, B. S. (1994). A double-moment multiple-phase four-class bulk ice scheme. Part I: Description. *Journal of the Atmospheric Sciences*, *51*(2), 249–280. https://doi.org/10.1175/1520-0469(1994)051<0249:admmpf>2.0.co;2

Fu, Q., Krueger, S. K., & Liou, K. (1995). Interactions of radiation and convection in simulated tropical cloud clusters. *Journal of the Atmospheric Sciences*, *52*(9), 1310–1328. https://doi.org/10.1175/1520-0469(1995)052<1310:ioraci>2.0.co;2

Gasparini, B., Blossey, P. N., Hartmann, D. L., Lin, G., & Fan, J. (2019). What drives the life cycle of tropical anvil clouds? *Journal of Advances in Modeling Earth Systems*, *11*(8), 2586–2605. https://doi.org/10.1029/2019ms001736

Grabowski, W. W. (2014). Extracting microphysical impacts in large-eddy simulations of shallow convection. *Journal of the Atmospheric Sciences*, *71*(12), 4493–4499. https://doi.org/10.1175/jas-d-14-0231.1

Grabowski, W. W. (2015). Untangling microphysical impacts on deep convection applying a novel modeling methodology. *Journal of the Atmospheric Sciences*, *72*(6), 2446–2464. https://doi.org/10.1175/jas-d-14-0307.1

Grim, J. A., McFarquhar, G. M., Rauber, R. M., Smith, A. M., & Jewett, B. F. (2009). Microphysical and thermodynamic structure and evolution of the trailing stratiform regions of mesoscale convective systems during BAMEX. Part II: Column model simulations. *Monthly Weather Review*, *137*(4), 1186–1205. https://doi.org/10.1175/2008mwr2505.1

Gustafson, W. I., Jr., Vogelmann, A. M., Li, Z., Cheng, X., Dumas, K. K., Endo, S., et al. (2020). The large-eddy simulation (LES) atmospheric radiation measurement (ARM) symbiotic simulation and observation (LASSO) activity for continental shallow convection. *Bulletin of the American Meteorological Society*, *101*(4), E462–E479. https://doi.org/10.1175/bams-d-19-0065.1

Hanisco, T. F., Lanzendorf, E., Wennberg, P., Perkins, K., Stimpfle, R., Voss, P., et al. (2001). Sources, sinks, and the distribution of OH in the lower stratosphere. *The Journal of Physical Chemistry A*, *105*(9), 1543–1553. https://doi.org/10.1021/jp002334g

Hartmann, D. L., & Berry, S. E. (2017). The balanced radiative effect of tropical anvil clouds. *Journal of Geophysical Research: Atmospheres*, *122*(9), 5003–5020. https://doi.org/10.1002/2017jd026460

Homeyer, C. R., McAuliffe, J. D., & Bedka, K. M. (2017). On the development of above-anvil cirrus plumes in extratropical convection. *Journal of the Atmospheric Sciences*, *74*(5), 1617–1633. https://doi.org/10.1175/jas-d-16-0269.1

Houze, R. A., Jr. (2004). Mesoscale convective systems. *Reviews of Geophysics*, *42*(4). https://doi.org/10.1029/2004RG000150

Jensen, A. A., Harrington, J. Y., & Morrison, H. (2018a). Impacts of ice particle shape and density evolution on the distribution of orographic precipitation. *Journal of the Atmospheric Sciences*, *75*(9), 3095–3114. https://doi.org/10.1175/jas-d-17-0400.1

Jensen, A. A., Harrington, J. Y., & Morrison, H. (2018b). Microphysical characteristics of squall-line stratiform precipitation and transition zones simulated using an ice particle property-evolving model. *Monthly Weather Review*, *146*(3), 723–743. https://doi.org/10.1175/mwr-d-17-0215.1

Jensen, A. A., Harrington, J. Y., Morrison, H., & Milbrandt, J. A. (2017). Predicting ice shape evolution in a bulk microphysics model. *Journal of the Atmospheric Sciences*, *74*(6), 2081–2104. https://doi.org/10.1175/jas-d-16-0350.1

Jensen, E., Pan, L. L., Honomichl, S., Diskin, G. S., Krämer, M., Spelten, N., et al. (2020). Assessment of observational evidence for direct convective hydration of the lower stratosphere. *Journal of Geophysical Research: Atmospheres*, *125*(15), e2020JD032793. https://doi.org/10.1029/2020jd032793

Kawashima, M. (2021). A numerical study of cirrus bands and low-static-stability layers associated with tropical cyclone outflow. *Journal of the Atmospheric Sciences*, *78*(11), 3691–3716. https://doi.org/10.1175/jas-d-21-0047.1

Keeler, E., & Burk, K. (2001). *Balloon-borne sounding system (SONDEWNPN)*. Atmospheric Radiation Measurement (ARM) User Facility. https://doi.org/10.5439/1595321

Khaykin, S. M., Moyer, E., Krämer, M., Clouser, B., Bucci, S., Legras, B., et al. (2022). Persistence of moist plumes from overshooting convection in the Asian monsoon anticyclone. *Atmospheric Chemistry and Physics*, *22*(5), 3169–3189. https://doi.org/10.5194/acp-22-3169-2022

Khaykin, S. M., Pommereau, J.-P., Riviere, E. D., Held, G., Ploeger, F., Ghysels, M., et al. (2016). Evidence of horizontal and vertical transport of water in the Southern Hemisphere tropical tropopause layer (TTL) from high-resolution balloon observations. *Atmospheric Chemistry and Physics*, *16*(18), 12273–12286. https://doi.org/10.5194/acp-16-12273-2016

Khordakova, D., Rolf, C., Grooß, J.-U., Müller, R., Konopka, P., Wieser, A., et al. (2022). A case study on the impact of severe convective storms on the water vapor mixing ratio in the lower mid-latitude stratosphere observed in 2019 over Europe. *Atmospheric Chemistry and Physics*, *22*(2), 1059–1079. https://doi.org/10.5194/acp-22-1059-2022

Labbouz, L., Kipling, Z., Stier, P., & Protat, A. (2018). How well can we represent the spectrum of convective clouds in a climate model? Comparisons between internal parameterization variables and radar observations. *Journal of the Atmospheric Sciences*, *75*(5), 1509–1524. https://doi.org/10.1175/jas-d-17-0191.1

Lin, L., Fu, Q., Liu, X., Shan, Y., Giangrande, S. E., Elsaesser, G. S., et al. (2021). Improved convective ice microphysics parameterization in the NCAR CAM model. *Journal of Geophysical Research: Atmospheres*, *126*(9), e2020JD034157. https://doi.org/10.1029/2020jd034157

Mansell, E. R., & Ziegler, C. L. (2013). Aerosol effects on simulated storm electrification and precipitation in a two-moment bulk microphysics model. *Journal of the Atmospheric Sciences*, *70*(7), 2032–2050. https://doi.org/10.1175/jas-d-12-0264.1

Mansell, E. R., Ziegler, C. L., & Bruning, E. C. (2010). Simulated electrification of a small thunderstorm with two-moment bulk microphysics. *Journal of the Atmospheric Sciences*, *67*(1), 171–194. https://doi.org/10.1175/2009jas2965.1

Moeng, C.-H., & Sullivan, P. P. (2015). Large-eddy simulation. *Encyclopedia of Atmospheric Sciences*, *2*, 232–240.

Morrison, H., & Milbrandt, J. A. (2015). Parameterization of cloud microphysics based on the prediction of bulk ice particle properties. Part I: Scheme description and idealized tests. *Journal of the Atmospheric Sciences*, *72*(1), 287–311. https://doi.org/10.1175/jas-d-14-0065.1

Morrison, H., Thompson, G., & Tatarskii, V. (2009). Impact of cloud microphysics on the development of trailing stratiform precipitation in a simulated squall line: Comparison of one-and two-moment schemes. *Monthly Weather Review*, *137*(3), 991–1007. https://doi.org/10.1175/2008mwr2556.1

Ovchinnikov, M., Fast, J. D., Berg, L. K., Gustafson, W. I., Jr., Chen, J., Sakaguchi, K., & Xiao, H. (2022). Effects of horizontal resolution, domain size, boundary conditions, and surface heterogeneity on coarse LES of a convective boundary layer. *Monthly Weather Review*, *150*(6), 1397–1415. https://doi.org/10.1175/mwr-d-21-0244.1

Pandey, A. (2023). *WRF deep convection sensitivity to microphysics parameterization (Version V1)*. Harvard Dataverse. https://doi.org/10.7910/DVN/EPZHOB

Petch, J. C. (2006). Sensitivity studies of developing convection in a cloud-resolving model. *Quarterly Journal of the Royal Meteorological Society*, *132*(615), 345–358. https://doi.org/10.1256/qj.05.71

Phillips, V. T. J., & Donner, L. J. (2006). Cloud microphysics, radiation and vertical velocities in two- and three-dimensional simulations of deep convection. *Quarterly Journal of the Royal Meteorological Society*, *132*(621C), 3011–3033. https://doi.org/10.1256/qj.05.171

Phoenix, D. B., Homeyer, C. R., & Barth, M. C. (2017). Sensitivity of simulated convection-driven stratosphere-troposphere exchange in WRF-Chem to the choice of physical and chemical parameterization. *Earth and Space Science*, *4*(8), 454–471. https://doi.org/10.1002/2017ea000287

Potter, B. E., & Holton, J. R. (1995). The role of monsoon convection in the dehydration of the lower tropical stratosphere. *Journal of the Atmospheric Sciences*, *52*(8), 1034–1050. https://doi.org/10.1175/1520-0469(1995)052<1034:tromci>2.0.co;2

Powers, J. G., Klemp, J. B., Skamarock, W. C., Davis, C. A., Dudhia, J., Gill, D. O., et al. (2017). The weather research and forecasting model: Overview, system efforts, and future directions. *Bulletin of the American Meteorological Society*, *98*(8), 1717–1737. https://doi.org/10.1175/bams-d-15-00308.1

Qu, Z., Huang, Y., Vaillancourt, P. A., Cole, J. N., Milbrandt, J. A., Yau, M.-K., et al. (2020). Simulation of convective moistening of the extra-tropical lower stratosphere using a numerical weather prediction model. *Atmospheric Chemistry and Physics*, *20*(4), 2143–2159. https://doi.org/10.5194/acp-20-2143-2020

Randel, W., & Park, M. (2019). Diagnosing observed stratospheric water vapor relationships to the cold point tropical tropopause. *Journal of Geophysical Research: Atmospheres*, *124*(13), 7018–7033. https://doi.org/10.1029/2019jd030648

Schmidt, C. T., & Garrett, T. J. (2013). A simple framework for the dynamic response of cirrus clouds to local diabatic radiative heating. *Journal of the Atmospheric Sciences*, *70*(5), 1409–1422. https://doi.org/10.1175/jas-d-12-056.1

Shan, Y., Wilcox, E. M., Gao, L., Lin, L., Mitchell, D. L., Yin, Y., et al. (2020). Evaluating errors in gamma-function representations of the raindrop size distribution: A method for determining the optimal parameter set for use in bulk microphysics schemes. *Journal of the Atmospheric Sciences*, *77*(2), 513–529. https://doi.org/10.1175/jas-d-18-0259.1

Shindell, D. T. (2001). Climate and ozone response to increased stratospheric water vapor. *Geophysical Research Letters*, *28*(8), 1551–1554. https://doi.org/10.1029/1999gl011197

Skamarock, W. C., Klemp, J. B., Dudhia, J., Gill, D. O., Liu, Z., Berner, J., et al. (2019). *A description of the advanced research WRF model version 4*. National Center for Atmospheric Research.

Smith, J. B., Wilmouth, D. M., Bedka, K. M., Bowman, K. P., Homeyer, C. R., Dykema, J. A., et al. (2017). A case study of convectively sourced water vapor observed in the overworld stratosphere over the United States. *Journal of Geophysical Research: Atmospheres*, *122*(17), 9529–9554. https://doi.org/10.1002/2017jd026831

Sokol, A. B., & Hartmann, D. L. (2020). Tropical anvil clouds: Radiative driving toward a preferred state. *Journal of Geophysical Research: Atmospheres*, *125*(21). https://doi.org/10.1029/2020jd033107

Straka, J. M. (2009). *Cloud and precipitation microphysics: Principles and parameterizations*. Cambridge University Press.

Tao, W. K., Wu, D., Lang, S., Chern, J. D., Peters-Lidard, C., Fridlind, A., & Matsui, T. (2016). High-resolution NU-WRF simulations of a deep convective-precipitation system during MC3E: Further improvements and comparisons between Goddard microphysics schemes and observations. *Journal of Geophysical Research: Atmospheres*, *121*(3), 1278–1305. https://doi.org/10.1002/2015jd023986

Tapiador, F. J., Sánchez, J.-L., & García-Ortega, E. (2019). Empirical values and assumptions in the microphysics of numerical models. *Atmospheric Research*, *215*, 214–238. https://doi.org/10.1016/j.atmosres.2018.09.010

Thompson, G., & Eidhammer, T. (2014). A study of aerosol impacts on clouds and precipitation development in a large winter cyclone. *Journal of the Atmospheric Sciences*, *71*(10), 3636–3658. https://doi.org/10.1175/jas-d-13-0305.1

Van Weverberg, K., Vogelmann, A. M., Morrison, H., & Milbrandt, J. A. (2012). Sensitivity of idealized squall-line simulations to the level of complexity used in two-moment bulk microphysics schemes. *Monthly Weather Review*, *140*(6), 1883–1907. https://doi.org/10.1175/mwr-d-11-00120.1

Wall, C. J., Norris, J. R., Gasparini, B., Smith, W. L., Thieman, M. M., & Sourdeval, O. (2020). Observational evidence that radiative heating modifies the life cycle of tropical anvil clouds. *Journal of Climate*, *33*(20), 8621–8640. https://doi.org/10.1175/jcli-d-20-0204.1

Xue, L., Bera, S., Chen, S., Choudhary, H., Dixit, S., Grabowski, W. W., et al. (2022). Progress and challenges in modeling dynamics–microphysics interactions: From the pi chamber to monsoon convection. *Bulletin of the American Meteorological Society*, *103*(5), E1413–E1420. https://doi.org/10.1175/bams-d-22-0018.1

Xue, L., Fan, J., Lebo, Z. J., Wu, W., Morrison, H., Grabowski, W. W., et al. (2017). Idealized simulations of a squall line from the MC3E field campaign applying three bin microphysics schemes: Dynamic and thermodynamic structure. *Monthly Weather Review*, *145*(12), 4789–4812. https://doi.org/10.1175/mwr-d-16-0385.1

Yu, W., Dessler, A. E., Park, M., & Jensen, E. J. (2020). Influence of convection on stratospheric water vapor in the North American monsoon region. *Atmospheric Chemistry and Physics*, *20*(20), 12153–12161. https://doi.org/10.5194/acp-20-12153-2020